Technical Note: Method to Correlate Whole Specimen Histopathology of Radical Prostatectomy with Diagnostic MR Imaging

Deirdre M. McGrath[1], Jenny Lee[1], Warren D. Foltz[1], Navid Samavati[2], Michael A.S. Jewett[3], Theo van der Kwast[4], Peter Chung[5], Cynthia Ménard[5,6], Kristy K. Brock[7]

[1]Radiation Medicine Program, Princess Margaret Hospital, University Health Network, Toronto, Ontario M5G 2M9, Canada

[2]Institute of Biomaterials and Biomedical Engineering, University of Toronto, Toronto, Ontario M5S 3G9, Canada

[3]Departments of Surgery (Urology) and Surgical Oncology, Princess Margaret Cancer Centre, University Health Network and University of Toronto, Toronto, Ontario M5G 2M9, Canada

[4]Pathology Department, University Health Network, Toronto, Ontario M5G 2C4, Canada

[5]Radiation Medicine Program, Princess Margaret Hospital, University Health Network and the University of Toronto, Toronto, Ontario M5G 2M9, Canada

[6]Centre Hospitalier de l'Université de Montréal, 1058 Rue Saint-Denis, Montréal, QC H2X 3J4, Canada

[7]Department of Radiation Oncology, University of Michigan, Ann Arbor, MI, 48108

ABSTRACT

Purpose: Validation of MRI-guided tumor boundary delineation for targeted prostate cancer therapy is achieved via correlation with gold-standard histopathology of radical prostatectomy specimens. Challenges to accurate correlation include matching the pathology sectioning plane with the *in vivo* imaging slice plane and correction for the deformation that occurs between *in vivo* imaging and histology. A methodology is presented for matching of the histological sectioning angle and position to the *in vivo* imaging slices.

Methods: Patients (n=4) with biochemical failure following external beam radiotherapy underwent diagnostic MRI to confirm localized recurrence of prostate cancer, followed by salvage radical prostatectomy. High resolution 3-D MRI of the *ex vivo* specimens was acquired to determine the pathology sectioning angle that best matched the *in vivo* imaging slice plane, using matching anatomical features and implanted fiducials. A novel sectioning device was developed to guide sectioning at the correct angle, and to assist the insertion of reference dye marks to aid in histopathology reconstruction.

Results: The percentage difference in the positioning of the urethra in the *ex vivo* pathology sections compared to the positioning in *in vivo* images was reduced from 34% to 7% through slicing at the best match angle. Reference dye marks were generated, which were visible in *ex vivo* imaging, in the tissue sections before and after processing, and in histology sections.

Conclusions: The method achieved an almost five-fold reduction in the slice-matching error, and is readily implementable in combination with standard MRI technology. The

technique will be employed to generate datasets for correlation of whole-specimen prostate histopathology with *in vivo* diagnostic MRI using 3-D deformable registration, allowing assessment of the sensitivity and specificity of MRI parameters for prostate cancer. Although developed specifically for prostate, the method is readily adaptable to other types of whole tissue specimen, such as mastectomy or liver resection.

Keywords: Pathology correlation; Histopathology; Prostate cancer; Magnetic resonance imaging; Registration; MRI-guided targeted therapy

I. INTRODUCTION

MRI has been demonstrated as a powerful tool for mapping the spatial extent of prostate cancer (PCa) for targeted therapy such as high dose rate brachytherapy[1] and MRI-guided biopsy[2], e.g., T_2-weighted (T2w) signal[3], and parameters from diffusion-weighted imaging (DWI)[3] and dynamic contrast enhanced MRI (DCE-MRI)[4]. However, the sensitivity and specificity of imaging parameters is determined by comparison with the gold-standard of histology. Retrospective evaluation can be made after radical prostatectomy, by correlation with a digital reconstruction of whole-mount histopathology[5]. This task is highly challenging, as deformation occurs from multiple influences between the *in vivo* state and histology[6], and it can be difficult to relate the anatomy of an *ex vivo* specimen to its *in vivo* orientation. Precise slice matching to *in vivo* imaging is critical, as the foci of early stage PCa are likely to be smaller than the pathology section width (typically 3 mm). This work presents a robust and readily implementable methodology for correlation of whole mount prostate histopathology with *in vivo* imaging, using intermediate *ex vivo* MRI

to determine the pathology sectioning plane, while employing a novel in-house developed sectioning device to guide slicing in this plane. The sectioning device also facilitates the insertion of dye-tracks to guide reconstruction of the 3-D histopathology volume, and reference dye marks to verify the accuracy of the pathology slice planes. An initial clinical evaluation of the methodology is presented.

II. METHODS

The workflow for the methodology involved a sequence of *in vivo* and *ex vivo* imaging and correlation techniques [Fig. 1].

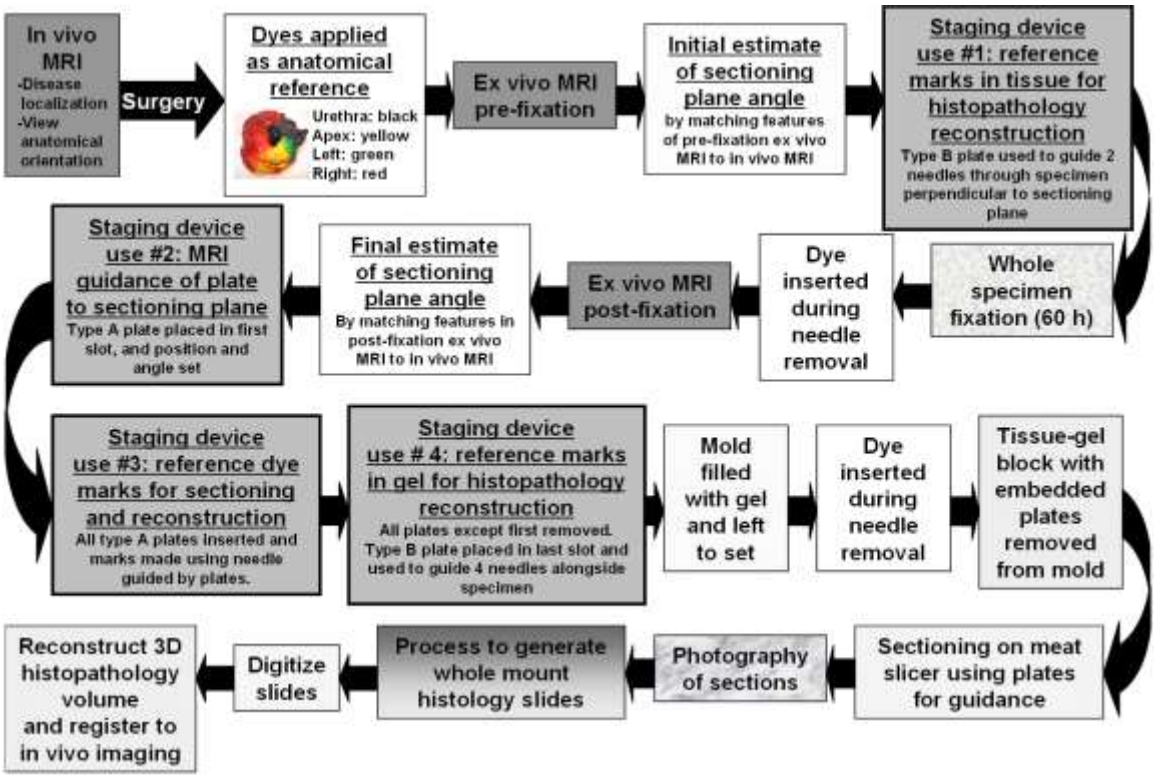

FIG. 1. Pathology correlation workflow. *Ex vivo* MRI of the specimen determines the pathology sectioning angle for best match with *in vivo* imaging. A sectioning device is employed in four steps, to guide pathology sectioning and create reference marks for histopathology reconstruction.

II.A. Patient recruitment

Prostate cancer patients (n=4) with biochemical failure after radiotherapy were enrolled in an institutional Research Ethics Board approved prospective clinical trial to map sites of local recurrence. Subsequent to a confirmed diagnosis from MRI and MR-guided biopsy, patients proceeded to radical prostatectomy.

II.B. *In vivo* imaging

Patients were imaged on a 1.5-tesla (T) MRI scanner (GE Signa Infinity) with a pelvic coil and an endorectal coil (MEDRAD MRInnervu). To minimize prostate deformation, the balloon of the endorectal coil was not inflated. The imaging examination included DWI, DCE-MRI, and T_2-weighted (T2w) imaging. The T2w imaging was a conventional diagnostic axial fast spin echo (FSE) acquisition: echo time (TE) = 102 ms; repetition time (TR) = 4650 ms; echo train length (ETL) = 16; field of view (FOV) = 140 $\times$ 140 mm^2, imaging matrix = 512 $\times$ 512; pixel in-plane dimension = 0.273 $\times$ 0.273 mm^2, slice thickness = 3 mm. Imaging was acquired axial to the endorectal coil. The areas suspicious for cancer were selected on the images by the oncologist (CM) using MIPAV (NIH, Bethesda, MD), on the basis of reduced T2w signal and evidence of extra-capsular extension.

II.C. Post-surgery anatomical marking with tissue dye

The surfaces of the prostate specimens were marked with tissue dye as a reference of anatomical orientation: apex = yellow; right side = red; left side = green; and black dye was inserted through the urethra.

II.D. High resolution MRI of *ex vivo* prostate at 7 T

To estimate the pathology sectioning angle and to determine the deformation during fixation, the *ex vivo* prostate was MRI scanned pre- and post-fixation. To prevent MRI susceptibility artifacts at air-tissue boundaries, the specimen was embedded in a block (7 $\times$ 7 $\times$ 7 cm^3) of gel (4% gelatin, 1.5% agarose), resting flat on the posterior surface above 1 cm of gel, and such that the axes of the specimen and block were aligned. The block was imaged in a 7-T preclinical MRI scanner (70/30 BioSpec, Bruker, Ettlingen, Germany), using a quadrature volume resonator (15.5 cm inner diameter) for transmission and reception. High magnetic field strength facilitated access to higher signal to noise ratios at high resolution, for enhanced anatomical mapping. A spin-echo sequence, Rapid Acquisition with Relaxation Enhancement (RARE) was used to obtain a T2w 3-D isotropic high-resolution acquisition of the block. The sequence parameters were: TE = 68 ms; TR= 2400 ms, ETL = 16: FOV = 70 $\times$ 70 $\times$ 70 mm^3, imaging matrix = 233 $\times$ 233 $\times$ 233; voxel dimension = 0.3 $\times$ 0.3 $\times$ 0.3 mm^3 (approximately matching the *in vivo* in-plane voxel dimension). The scan acquisition time was about 2 h. Post-fixation, TE was reduced to 40 ms, to compensate for fixation-mediated reduction in the transverse relaxation time, T_2[9].

II.E. Pathology sectioning angle estimation from *ex vivo* MRI

Prostate specimens are typically positioned on the posterior surface (closest to the rectum) prior to sectioning. Therefore, to match sectioning to *in vivo* imaging, estimation must be made of the angle in the anterior-posterior direction between the posterior

surface and the coil axis (axis of imaging), denoted α_1, and also the left-right angle between the main axes of the prostate and coil, denoted α_2. Angles α_1 and α_2 were initially estimated using the pre-fixation *ex vivo* MRI data, and updated post-fixation. The oncologist (CM) contoured the prostate boundaries and identified salient anatomical features on all images using Matlab (The MathWorks, Natick, MA). Three implanted gold seed fiducials (length 3-5 mm, diameter 1 mm) were visible as focal hypointensities for three patients (#2-4), both *in vivo* and *ex vivo*. Contours were drawn around each marker artifact, allowing centroid calculation. A 3-D rotational transform between the *in vivo* and *ex vivo* states was calculated from the marker centroids, which provided estimates of α_1 and α_2.

Implanted fiducial markers were not visible for patient #1, necessitating the use of distance metrics for angle estimation [Fig. 2]. Four distances were measured to the center of the urethra in corresponding *in vivo* and *ex vivo* slices: d1: the distance from the anterior surface; d2: from the posterior surface; d3: from the left surface; d4: from the right surface. The ratios of these distances were calculated:

$$r_{1,2} = \frac{d_1}{d_2} \quad r_{3,4} = \frac{d_3}{d_4} \tag{1}$$

The axial (to the posterior surface) *ex vivo* data was digitally resampled at varying axial oblique angles (α_1) from -30º to + 30º in steps of 5º, and down-sampled to create 3-mm thick slices, to match the *in vivo* slices. The α_1 was identified that minimized the mean square difference between *in vivo* and *ex vivo* ratios. For final refinement, α_1 was varied through increments of 1º in the vicinity of the minimum. Angle α_2 was determined by rotation of the α_1-rotated data through increments of 1º from -5º to +5º.

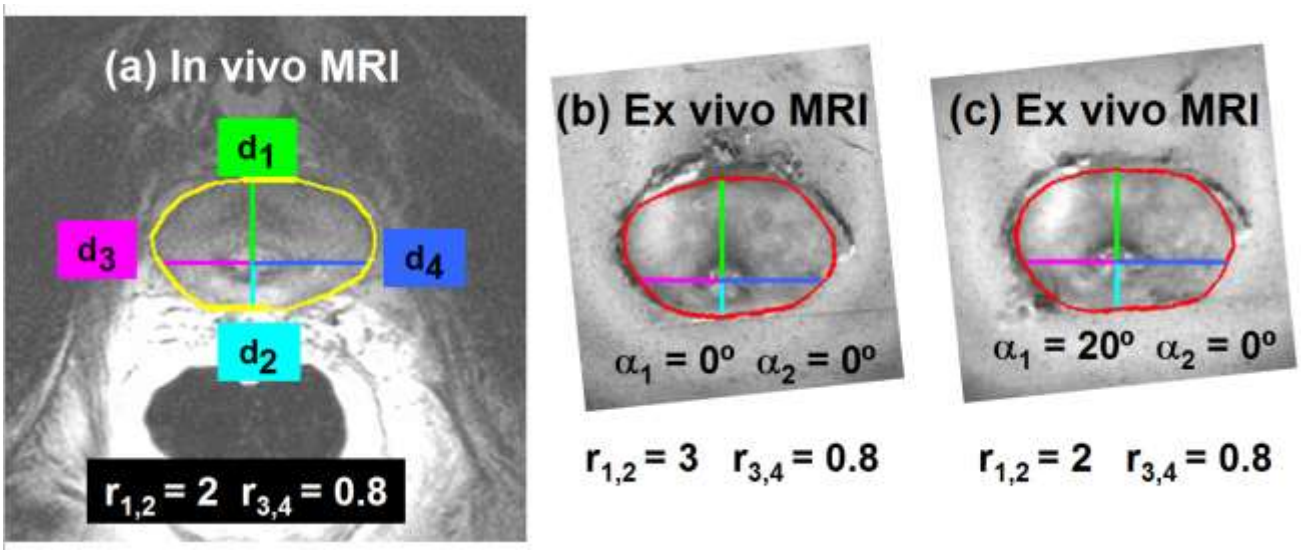

FIG.2. Estimating α_1 and α_2 by comparison of distance metrics between *in vivo* and (pre-fixation) *ex vivo* MRI data sets. (a) On the *in vivo* image distances are measured between the center of the urethra and the anterior (d_1), posterior (d_2), left (d_3) and right (d_4) edges, from which the ratios $r_{1,2}$ and $r_{3,4}$ are calculated. (b) The metrics are measured on the *ex vivo* MRI slice and the ratios compared with *in vivo* data. (An in-plane rotation was also required to compensate for rotation of the specimen caused by extraprostatic tissue on the posterior surface.) (c) The *ex vivo* data rotated by $\alpha_1 = 20^o$ gives the best match to *in vivo* ratios.

II.F Sectioning device

A sectioning device [Fig. 3] was designed for MRI-guided matching of the sectioning planes to *in vivo* imaging. It consisted of an acrylic mold with detachable sides, and a series of attachments and guidance plates made from polycarbonate (ABS blend), which were generated by fast prototyping using a Stratasys Vantage 3-D printer (Stratasys, MN). The hypodermic needles employed were 21G and 12 cm long (B.Braun Melsungen AG, Germany), and the tissue dye (Bradley Products, Inc., MN) was diluted in a 1:5 ratio with ultrasound (U/S) gel, to limit diffusion and leakage.

II.G. Sectioning device use #1: Insertion of needle tracks through the tissue

On completion of the fresh state *ex vivo* MRI, α_1 and α_2 were estimated. The specimen was removed from gel, and two needles were inserted in the tissue perpendicular to the determined sectioning plane [Fig 3(c)], which were left in place during fixation to create holes that would be visible in histology. For fixation the specimen was submersed for 60 h in 10% neutral buffered formaldehyde solution (formalin). Once removed from formalin, dye was inserted during needle removal, to help distinguish the needle marks from other features.

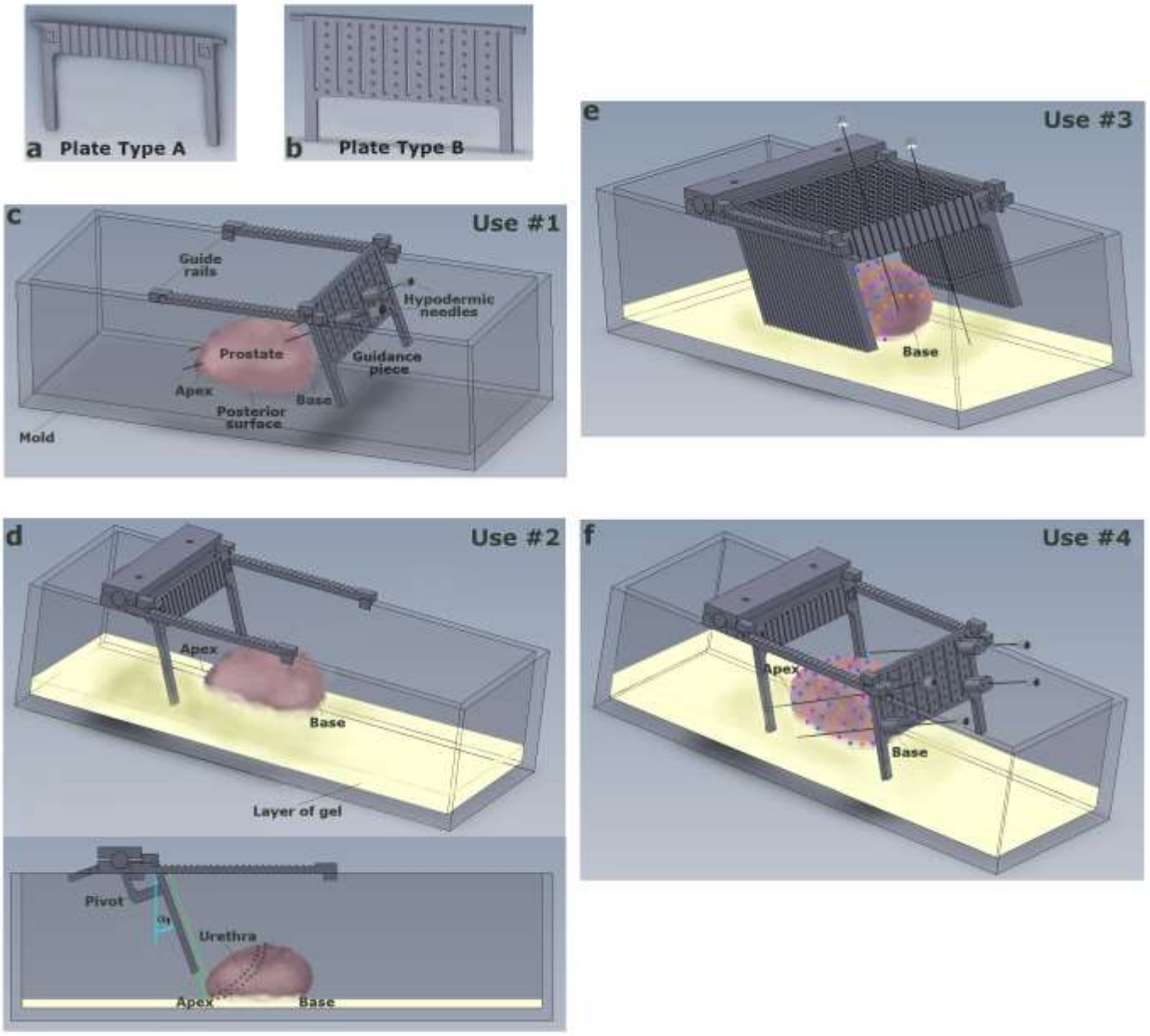

FIG.3. Sectioning device. (a) Plate type A (width = 9 cm, height = 5.5 cm, thickness = 3 mm) with 1-mm deep grooves for needle-guidance, and to create MR-visible reference tracks when filled with ultrasound gel. (b) Plate type B (same dimensions as type A) with slots for guiding needles through plate. (c-f) Device includes a rectangular mold (length = 25 cm, width = 10 cm), and guide rails for holding plates, with a pivot to set the angle. (c) Use #1: guiding needles through type B plate and perpendicular to the slicing plane. (d) Use #2: setting the angle of the type A plate to the slicing angle. (Side view depicts the urethra trajectory.) (e) Use #3: all type A plates are fitted at the slicing

angle, and needles are guided into tissue surface to create reference dye marks for sectioning. (f) Use #4: Type B plate is fitted to the last slot and at the same angle, and needles are positioned through the plate to create tracks through the gel that will embed the tissue.

II.H. Sectioning device use #2: Setting angle and position of the sectioning guidance plate

On completion of the fixed state *ex vivo* MRI, α_1 and α_2 were updated. The mold was pre-set with a 1-cm gel layer, upon which the specimen was placed on its posterior surface. (α_2 was not found to differ from zero for any specimen, however in the instance where α_2 is non-zero, a protractor may be employed to position the specimen accordingly.) For immobilization, another 1-cm layer of gel was poured around the specimen and allowed to set.

The pathology section thickness matched the *in vivo* MRI slice thickness (3 mm). For optimum sampling of disease margins at the apex, the width of the first section at the apex should be close to 3 mm. Hence, the objective was to position the first plate in the 3-mm slice immediately before the first slice containing tissue [Fig. 3d]. A set of 1-mm thick T2w MR imaging slices were acquired at α_1. It was deemed that the plate position and angle was correct when the U/S-gel filled grooves were visible in the last 1-mm slice before the apex.

II.I. Sectioning device use #3: Insertion of dye marks at the sectioning positions

All the type-A plates were fitted and set to α_1 [Fig.3(e)]. A needle was guided along the grooves in each plate to insert dye markers of about 1 cm in depth into the tissue, by first depositing a small quantity on the surface, followed by slowly inserting the needle while

not applying pressure to the syringe. Marks were made at 5-mm intervals across the slicing planes, which were separated by 3 mm. The dye color was varied between plates in a repeating sequence of three colors, to distinguish neighboring planes. On completion, all plates, with the exception of the first, were removed, and the last plate was replaced by a type-B plate. These two plates would remain in place to guide pathology sectioning, and furthermore the type-B plate would be used for the work described in the next section.

II.J Sectioning device use #4: Insertion of needle tracks through the gel

Four needles were pushed through the type-B plate and positioned alongside the tissue [Fig.3(f)]. These would create tracks in the embedding gel, which would guide stacking of the digital images of the tissue sections during histopathology reconstruction. The mold with the specimen, plates and needles in place was filled with gel and refrigerated overnight. To increase track visibility, dye was deposited during needle removal.

II.K Pathology sectioning

To prepare the specimen for sectioning, first the sides of the mold were detached from the gel block in which the specimen was embedded, and the guide rails were also removed. The specimen would remain embedded in gel during sectioning. Furthermore the two guidance plates (see section II.I) would remain embedded in the gel with the specimen, to help guide sectioning. A rotary blade meat slicer was used for sectioning and the sectioning angle on the slicer was set by use of a rectangular wedge of gel, which was prepared at the best match angle α_1. The gel block containing the specimen

was placed on top of the wedge block, and both were trimmed so that the combined cutting edge was parallel to the embedded plates. The block and wedge were placed on the holding tray of the slicer so that the apex would be sliced first. The pathologist (TvdK) performed all histological sectioning. Once slicing had reached the first (type A) plate, the block and wedge were removed from the slicer and the plate was detached. Some gel protruded from where the rectangular opening in the plate had been, and this was carefully trimmed by hand to create a tight fit with the back plate of the slicer. The block and wedge were repositioned on the slicer, verifying that the slice plane was parallel to the remaining plate. The next slice consisted of the first slice of the apex, and slicing continued for the whole specimen. The sections were ordered in sequence during slicing, with the surrounding gel kept in place, and were digitally captured at high resolution using a camera mounted at a fixed height, while resting on a 1-mm spaced grid to indicate the dimensions.

II.L. Histopathology Processing

The tissue sections were processed in a histoprocessor, embedded in paraffin and sliced on a sledge microtome to produce one 5-μm whole-mount histology slide section from the top of each block, which was stained with Hematoxylin and Eosin (H&E). The slides were digitized at 5 μm resolution on a TISSUEscope™ 4000 (Biomedical Photometrics Inc., ON, Canada) and digitally annotated by the pathologist using Aperio Imagescope software (Aperio Technologies, Inc., CA).

III. Results

III.A Pathology slicing angle estimation from *ex vivo* MRI

For specimen #1, estimates of α_1 and α_2 were 20º and 0º respectively before fixation, and were unchanged after fixation. The estimated angles for specimens #2-4 (Table I) (i.e., with fiducial markers) were similar to those of specimen #1, and approximately consistent before and after fixation, with an average α_1 of 17º both pre- and post-fixation, while α_2 was 0º for all specimens. Angle variation after fixation is likely due to tissue deformation. A possible added influence is pressure from the plate guiding the needles during use #1, and care was taken to avoid this (subsequent to the differing angle result of specimen #2), by ensuring that the plate was supported underneath.

The *in vivo* MRI $r_{1,2}$ values for an example slice near the apex were compared with the ratios in post-fixation *ex vivo* MRI axial to the posterior surface, post-fixation *ex vivo* MRI resampled at α_1, and the tissue slice photograph. The $r_{1,2}$ errors were calculated from estimated uncertainties of 1 mm for the tissue edge and the urethra center. For specimen #1 the $r_{1,2}$ ratio measured on *in vivo* MRI was 1.9±0.4, and on the *ex vivo* post-fixation slice without digital resampling $r_{1,2}$ was 2.6±0.6 (37% difference). After digital resampling of the *ex vivo* data, the $r_{1,2}$ ratio was 1.9±0.4, which matched the *in vivo* ratio. After sectioning, $r_{1,2}$ on the tissue slice photograph was 1.8±0.4; a difference of -5% with the *in vivo* $r_{1,2}$. The ratios and percentages were similar for specimens #2-4 (Table II). A substantial improvement in spatial matching was achieved with resampling at α_1, i.e., the mean absolute percentage difference of $r_{1,2}$ was reduced from 34(±18)% to 12(±4)%.

Table I. Results of angle estimation from *ex vivo* MRI data for specimens #2-4

Specimen no.	Pre-fixation		Post-fixation	
	α_1	α_2	α_1	α_2
2	10º	0º	5º	0º
3	20º	0º	20º	0º
4	20º	0º	25º	0º
Mean(±std)	17(±6)º	0º	17(±10)º	0º

Table II. For specimens #2-4, $r_{1,2}$ values for example matching slices near the apex for *in vivo* MRI, *ex vivo* MRI, *ex vivo* MRI resampled at α_1, and in the photographed tissue slices. For the *ex vivo* ratios, the percentage differences from the *in vivo* ratios are also listed.

Specimen no.	$r_{1,2}$ in vivo MRI	$r_{1,2}$ *ex vivo* MRI	% Δ ($r_{1,2}$ *ex vivo MRI* - $r_{1,2}$ *in vivo* MRI)	$r_{1,2}$ *ex vivo* MRI resampled at α_1	% Δ ($r_{1,2}$ *ex vivo* MRI resampled - $r_{1,2}$ *in vivo* MRI)	$r_{1,2}$ tissue slice	% Δ ($r_{1,2}$ tissue slice - $r_{1,2}$ *in vivo* MRI)
2	1.5±0.2	1.7±0.3	13%	1.6±0.3	7%	1.5±0.3	0%
3	1.6±0.3	2.3±0.5	44%	1.4±0.3	-13%	1.6±0.3	0%
4	2.0±0.4	2.9±0.7	45%	2.3±0.6	15%	1.6±0.3	-20%
Mean			34(±18)		12(±4)		7(±12)

absolute % Δ							

III.B The sectioning device

Use #1:

The dye tracks were visible in the post-fixation *ex vivo* MRI [Fig. 4(a)], and in the tissue sections [Fig. 4(b)]. While the dye was found to mostly wash away during the histology processing before paraffin embedding [Fig. 4(c)], the holes created by the needles were still clearly visible with some indication of the dye around the rim. Furthermore, these holes were visible on the histology sections [Fig.4(d)].

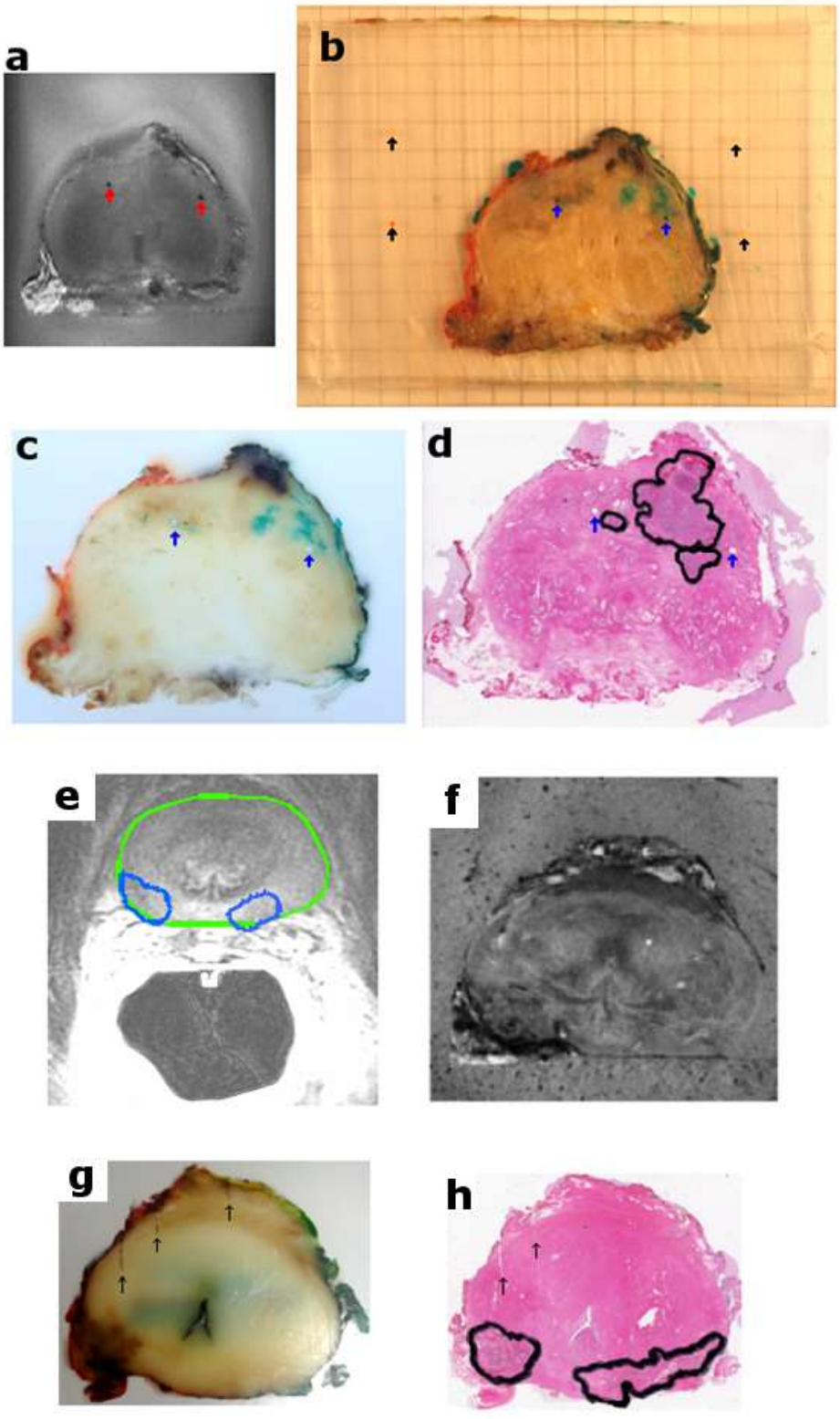
a
b
c
d
e
f
g
h

FIG 4. Matching images for MRI and histology. (a-d): Slice position towards prostate base. (e-h): Central slice position. (a) *Ex vivo* post-fixation MRI resampled at α_1. Red arrows indicate dye tracks from use #1. (b) Photograph of tissue section with gel. Blue arrows indicate dye tracks from use #1, while black arrows indicate dye tracks from use #4. (c) Paraffin block after removal of histology slide section. Arrows indicate holes corresponding to tissue dye tracks from use #1. (d) H&E stained histology slide with tumor areas marked by pathologist (black). Blue arrows indicate holes corresponding to dye tracks from use #1. Some residual gel is present around the tissue. (e) *In vivo* T2w MRI showing contour of prostate and tumor areas as determined by the oncologist. (f) *Ex vivo* pre-fixation MRI of matching slice resampled at α_1. (g) Paraffin block after removal of histology section. Arrows indicate the dye marks from use #3. (h) H&E stained histology slide with tumor areas marked by the pathologist (black). Arrows indicate tracks of marks from use #3.

Use #2:

The U/S gel in the grooves of the type-A plate was predominantly visible in the last 1-mm slice before the apex. The uncertainty on the positioning of the 1-mm wide and 15-mm long grooves in a 1-mm wide imaging slice was estimated as half the depth of the groove, at 0.5 mm (i.e., partial volume averaging with neighboring slices). Therefore, the uncertainty on the setting of α_1 was arctan(0.5/15) = 1.9º. The average error on $r_{1,2}$ for specimens #2-4 for the tissue slice photographs was 7(±12)%, which is lower than the average error for the resampled *ex vivo* MRI (12(±4)%) (Table II), demonstrating that the step of setting the sectioning angle by use of the sectioning device did not inflate the errors.

Use #3:

The dye marks inserted at the planned sectioning positions were visible in some sections after slicing. Owing to variable pressure applied during sectioning on the slicer, the section thickness was found to vary slightly (typically between 2.9 and 3.1 mm) and these errors could accumulate through slicing, and hence sectioning did not always occur at the predefined positions. However, when visible it was possible to verify accuracy of the slice plane angle in the left-right direction, by comparing marker visibility on the left and right. The dye marks were found to be robust to all processing steps (cycles of formalin, ethanol, xylene and paraffin in the histoprocessor) to create the paraffin blocks [Fig.4(g)]. This added a further reference for the left-right angle during histology sectioning on the microtome. Needle tracks corresponding to these dye marks were visible on the histology slides [Fig. 4(h)].

Use #4:

The needle tracks made through the gel were visible on photography of the sections, with some of the dye remaining in the tracks [Fig.4(b)].

III.C Comparison of slices from *in vivo* to histology

Correlation of anatomical features was observed between *in vivo* MRI, *ex vivo* MRI, section photography, paraffin blocks and histology [Fig.4]. Furthermore, there was initial indication of coincidence of disease margins between diagnostic MRI [Fig.4(e)] and histology [Fig.4(h)]. Extraprostatic tissue removed with the prostate provided extra cross-referencing features for slice matching between *ex vivo* data. However, in histology this

extra tissue (sometimes combined with residual gel from the block) tended to fragment [Figs. 4(d) and 4(h)].

IV. DISCUSSION

IV.A Comparison with other methods

In the prostate the urethra follows an arc-shaped path [Fig.3(d)], and therefore slicing perpendicular to an arbitrary axis of the urethra[7,8] can give rise to an angle mismatch of as much as 15º [7]. Langer et al[10] imaged *ex vivo* specimens at multiple axial oblique angles in increments of 5º to match *in vivo* imaging. In another study, an organ mold was designed from *in vivo* images, in which the specimen was fixed, imaged and sliced[11]. However, tissue can deform in the mold during fixation. Image-guided magnetically tracked probes have also been used to indicate the sectioning plane on the *ex vivo* specimen[6]. In contrast, the method presented here is readily implementable with standard MRI technology.

IV.B Pathology slice angle estimation

Angle estimation from *in vivo* imaging was inaccurate, as the 3-mm thick imaging slices provided very approximate information on the prostate shape, and it was not known how the *ex vivo* specimen would align on the posterior surface. The angle estimates from *ex vivo* imaging were generally similar between specimens, suggesting a common anatomical orientation and a predictable compression by the coil. For the distance metric approach, errors were estimated based on a 1 mm uncertainty in contour and feature selection. For the gold seeds method, the uncertainty was dependent on the artifact

boundary selection. However, as the artifact dimensions vary between frequency-encode and phase-encode directions, and with magnetic field strength and readout bandwidth, the overall uncertainty was difficult to assess, and will be the subject of future work. However, further studies are required with larger numbers of specimens to fully explore the variability of prostate anatomy between individuals and the accuracy of pathology slice matching using this methodology.

IV.C Benefits of the sectioning device

The device provided a means of guiding pathology sectioning at the angles and positions which were estimated to best match the *in vivo* imaging planes. Even though prostate tissue is likely to undergo deformation from multiple influences between *in vivo* imaging and histology (i.e., deformable registration is included in the proposed pipeline to reduce errors from these effects [Fig.1]), matching of the pathology slice angles to *in vivo* imaging is still a critically important step in the process. Given that the dimension of the foci of early stage PCa could be less than the pathology tissue slice thickness (3 mm), and that typically only a single histology slide is created from the top of each pathology section, it is vital to match the histology slice angles with the best estimates of the *in vivo* imaging angles. The device also ensured an adequate width of the first tissue section, which permits more precise sampling at the margins (e.g., with multiple-step histology).

The dye tracks through the tissue and gel provided a reference for histopathology reconstruction, and the tissue tracks could be used to assess deformation during processing. Although no needle deformation was discernable during needle insertion in the tissue or gel, slight deviations in the needle trajectory may occur. However, these

deviations might be detectable in the post-fixation MRI data, and examination of the data for these potential effects should be included in future implementations of this process. The dye marks at the planned sectioning positions indicated the slicing plane accuracy, and assisted histology slicing on the microtome.

The data obtained will be used in 3-D finite element modeling (FEM) biomechanical-based deformable registration[12,13,14] of the histopathology volume to the *in vivo* volume in a step-wise process through the tissue states: 1) histopathology to *ex vivo* fixed MRI; 2) the result of 1 to *ex vivo* fresh MRI; 3) the result of step 2 to *in vivo* MRI.

V. CONCLUSIONS

A methodology has been presented for correlation of whole-specimen prostate histopathology with *in vivo* diagnostic MRI. *Ex vivo* MRI was employed to determine the pathology sectioning angle, and a novel sectioning device was demonstrated as an important tool to guide sectioning, and to allow creation of reference dye marks to aid in histopathology reconstruction. The process is easily implemented with standard MRI technology, and is also readily adaptable to other tissue types, such as mastectomy, or liver resections. The data obtained will be used to register histopathology with *in vivo* imaging, to determine the sensitivity and specificity of diagnostic MRI parameters to prostate cancer.

ACKNOWLEDGEMENTS

This research was funded in part by a grant from the Ontario Institute for Cancer Research and in part by an NIH grant # 5R21CA121586-2. K.K.B. was supported as a

Cancer Care Ontario Research Chair. The authors would like to thank Matthew Filleti for technical assistance in development of the sectioning device, and Dr. Andrew Evans for pathology support.

415

REFERENCES

[1]C. Menard, R.C. Susil, P. Choyke, G.S. Gustafson, W. Kammerer, H. Ning, R.W. Millner, K.L. Ullman, N.S. Crouse, S. Smith, E. Lessard, J. Pouliot, V. Wright, E. McVeigh, C.N. Coleman, K.C. Camphausen, "MRI-guided HDR prostate brachytherapy in standard 1.5T scanner," Int. J. Radiat. Oncol., Biol., Phys. **59** (5), 1414-1423 (2004).

[2]C. Menard, D. Iupati, J. Lee, A. Simeonov, J. Abed, J. Publicover, P. Chung, A. Bayley, C. Catton, M. Milosevic, R. Bristow, G. Morton, P. Warde, K. Brock, M.A. Haider, "MRI and biopsy performance in delineating recurrent tumor boundaries after radiotherapy for prostate cancer," Proc. Intl. Soc. Mag. Res. Med. **19**, 3072 (2011).

[3]M.A. Haider, T.H. van der Kwast, J. Tanguay, A.J. Evans, A. Hashmi, G. Lockwood, J. Trachtenberg, "Combined T2-weighted and diffusion-weighted MRI for localization of prostate cancer," Am. J. Radiol. **189**, 323-328 (2007).

[4]M.A. Haider, P. Chung, J. Sweet, A. Toi, K. Jhaveri, C. Menard, P. Warde, J. Trachtenberg, G. Lockwood, M. Milosevic, "Dynamic contrast-enhanced magnetic resonance imaging for localization of recurrent prostate cancer after external beam radiotherapy," Int. J. Radiation Oncology Biol. Phys. **70** (2), 425-430 (2008).

[5]D.L. Langer, T.H. van der Kwast, A.J. Evans, J. Trachtenberg, B.C. Wilson, M.A. Haider, "Prostate cancer detection with multi-parametric MRI: logistic regression analysis of

quantitative T2, diffusion-weighted imaging, and dynamic contrast-enhanced MRI," J Magn Reson Imaging **30**, 327-334 (2009).

[6]A.D. Ward, C. Crukley, C. McKenzie, J. Montreuil, E. Gibson, J.A. Gomez, M. Moussa, G. Bauman, A. Fenster, "Registration of in vivo prostate magnetic resonance images to digital histopathology images," In Proc. MICCAI: International Conference on Medical Image Computing and Computer Assisted Intervenion, LNCS **6367**, 66-76 (2010).

[7]G.J. Jager, E.T.G. Ruijter, C.A. van de Kaa, J.J.M.C.H. de la Rosette, G.O.N. Oosterhof, J.R. Thornbury, J.O. Barentsz, "Local stagin of prostate cancer with endorectal MR imaging: correlation with histopathology," Am. J. Roent **166**, 845-852 (1996).

[8]A. Graser, A. Heuck, b. Sommer, J. Massmann, J. Scheidler, M. Reiser, U. Mueller-Lisse, "Per-sextant localization and staging or prostate cancer: correlation of imaging findings with whole-mount step section histopathology," Am. J. Roent **188**, (2007).

[9]C. Yong-Hing, A. Obenaus, R. Stryker, K. Tong, G. Sarty, "Magnetic resonance imaging and mathematical modeling of progressive formalin fixation of the human brain," Magn Res Med **54**, 324-332 (2005).

[10]D.L. Langer, T.H. van der Kwast, A.J. Evans, A. Plotkin, J. Trachtenberg, B.C. Wilson, M.A. Haider, "Prostate tissue composition and MR measurements: investigating the

relationships between ADC, T2, Ktrans, Ve and corresponding features," Radiology **255** (2), 485-494 (2010).

[11]V. Shah, T. Pohida, B. Turkbey, H. Mani, M. Merino, P.A. Pinto, P. Choyke, M. Bernardo, "A method for correlating in vivo prostate magnetic resonance imaging and histopathology using individualized magnetic resonance -based molds," Rev. Sci. Instrum. **80** (10), 104301 (2009).

[12]A. McNiven, J. Moseley, D.L. Langer, M.A. Haider, K.K. Brock, "Preliminary feasibility study: modeling 3D deformations of the prostate from whole-mount histology to in vivo MRI," Med Phys **36**, 2712 (2009).

[13]K. Brock, S. Ahmed, J. Moseley, C. Moulton, M. Guindi, M. Haider, S. Gallinger, L. Dawson, "Deformable registration for in vivo imaging and pathology correlation," Med Phys **33**, 1994 (2006).

[14]K.K. Brock, M.B. Sharpe, L.A. Dawson, S.M. Kim, D.A. Jaffray, "Accuracy of finite element model-based multi-organ deformable image registration," Med Phys **32** (6), 1647-1659 (2005).